Journal of *Marine Science and Engineering*

MDPI

Article

Experimental Study on Adaptive Backstepping Synchronous following Control and Thrust Allocation for a Dynamic Positioning Vessel

Changde Liu [1,2,*], Yufang Zhang [3], Min Gu [1,2], Longhui Zhang [1,2], Yanbin Teng [1,2] and Fang Tian [1,2]

[1] China Ship Scientific Research Center, Wuxi 214082, China
[2] Taihu Laboratory of Deepsea Technological Science, Wuxi 214082, China
[3] School of Control Technology, Wuxi Institute of Technology, Wuxi 214121, China
* Correspondence: liucd@cssrc.com.cn

Abstract: Cargo transfer vessels (CTVs) are designed to transfer cargo from a floating production storage and offloading (FPSO) unit into conventional tankers. The dynamic positioning system allows the CTV to maintain a safe position relative to the FPSO unit using a flexible cargo transmission pipe, and the CTV tows the tanker during operating conditions. The operation mode can be considered a synchronization tracking control problem. In this paper, a synchronization control strategy is presented based on the virtual leader–follower configuration and an adaptive backstepping control method. The position and heading of the following vessel are proven to be able to globally exponentially converge to the virtual ship by the contraction theorem. Then, the optimization problem of the desired thrust command from the controller is solved through an improved firefly algorithm, which fully considers the physical characteristics of the azimuth thruster and the thrust forbidden zone caused by hydrodynamic interference. To validate the effectiveness of the presented synchronous following strategy and thrust allocation algorithm, a scale model experiment is carried out under a sea state of 4 in a seakeeping basin. The experimental results show that the CTV can effectively maintain a safe distance of 100 m with a maximum deviation of 3.78 m and an average deviation of only 0.99 m in the wave heading 180°, which effectively verifies that the control strategy proposed in this paper can achieve safe and cooperative operation between the CTV and the FPSO unit. To verify the advantages of the SAF algorithm in the thrust allocation, the SQP algorithm and PSO algorithm are used to compare the experimental results. The SAF algorithm outperforms the SQP and PSO algorithms in longitudinal and lateral forces, with the R-squared (R^2) values of 0.9996 (yaw moment), 0.9878 (sway force), and 0.9596 (surge force) for the actual thrusts and control commands in the wave heading 180°. The experimental results can provide technical support to improve the safe operation of CTVs.

Keywords: dynamic positioning; virtual leader–follower; backstepping; synchronization; contraction theory; control allocation; model experiment

check for updates

Citation: Liu, C.; Zhang, Y.; Gu, M.; Zhang, L.; Teng, Y.; Tian, F. Experimental Study on Adaptive Backstepping Synchronous following Control and Thrust Allocation for a Dynamic Positioning Vessel. *J. Mar. Sci. Eng.* **2024**, *12*, 203. https://doi.org/10.3390/jmse12020203

Academic Editor: Mohamed Benbouzid

Received: 5 December 2023
Revised: 19 January 2024
Accepted: 19 January 2024
Published: 23 January 2024

1. Introduction

With the development of deep-sea oil and gas resource development technology, a brand-new concept of a deep-water dynamic positioning cargo transfer vessel has been proposed. The vessel is composed of a CTV equipped with a dynamic positioning (DP) system and a cargo transfer device onboard the CTV. The CTV performs the same role as a tanker and maintains position within the floating production storage and offloading (FPSO) unit. The offloading hose is passed from the FPSO to the CTV and it is connected. The cargo is then pumped to the tanker via the CTV using booster pumps. A corresponding safe working distance must be maintained between the CTV and the FPSO unit due to the limitations of the transfer device. The design of a strategy to synchronously control

the CTV and the FPSO unit under a towing state is important for improving the efficient operation of the CTV. A schematic diagram of the CTV operation is shown in Figure 1.

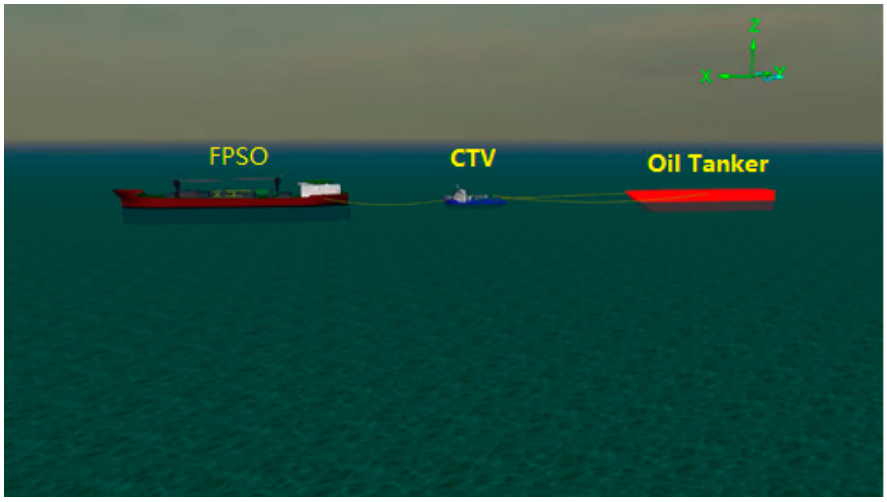

Figure 1. Schematic diagram of CTV operation with an FPSO unit and a tanker.

During cargo transfer between the CTV and the FPSO unit, the whole operation process can be regarded as a formation coordination control problem. At present, formation control strategies are mainly categorized into hybrid behavior-based formation control methods [1], virtual structure-based formation control methods [2] and leader–follower formation control methods. In actual operation processes, leader–follower formation control methods are widely used. Wu et al. [3] combined a leader–follower control strategy with a path planning strategy based on an artificial potential field method to propose a formation motion control method for unmanned surface vehicles (USVs) and designed a set of control laws for underactuated USVs. Wang et al. [4] proposed a fixed-time controller strategy based on the leader–follower mechanism and finite time disturbance observer. Shojaei et al. [5] proposed a leader–follower formation control method for underactuated surface vessels with actuator saturation. Cui et al. [6] proposed a leader–follower formation control for multiple underactuated autonomous underwater vehicles. To improve the tracking performance under uncertain sea conditions, a backstepping control with compensation control was designed [7]. Witkowska et al. [8] designed a course-keeping control system using a genetic algorithm and adaptive backstepping method. In recent years, with the development of intelligent technology, a variety of adaptive swarm formation control methods for unmanned vessels have emerged [9–11].

Most of the above research results are focused on underactuated control systems. Ships equipped with DP systems are generally equipped with tunnel thrusters, azimuth thrusters, and rudder propeller systems. When only used to control the three degrees of freedom in the ship's horizontal plane, the DP system is an overactuated system. Therefore, it can simultaneously control the horizontal, longitudinal, and heading positions in the horizontal plane. Sørensen [12] systematically summarized the DP control methods. In recent years, various improved algorithms for H-infinity control [13], backstepping control [14], sliding mode control [15], and nonlinear model predictive control [16,17] have emerged, and some control strategies have been applied to target point positioning models or full-scale ship experiments [18–20]. To achieve the synchronous control of DP vessels, Erick et al. [21] proposed a synchronization control strategy for underway replenishment, which realized the synchronization control of the supply vessels and the supplied vessels. However, hydrodynamic interactions between the two ships are crucial for the design of their automatic motion control systems; Miller [22] studied the interference of the forces and yaw moments between the two ships through the model tests. To achieve robustness to sea conditions, a leader–follower-based formation control problem was proposed for the

collision avoidance study of fully driven USVs, and adaptive control technology was used to estimate the uncertain parameters of environmental disturbances [23].

At present, most of the above existing DP control methods use Lyapunov stability theory to prove the stability of closed-loop systems [15–23]. However, the designed controller method has high requirements for the system equilibrium state information. With the emergence and perfection of contraction theory, the concept of virtual displacement has gradually been used to solve the problem of system stability. Guttorm [24] designed a DP vessel observer based on contraction theory, determined that the system is globally contracting, and verified the robustness of the control system by simulation. Zhang et al. [25] designed a DP control law based on contraction theory to address DP vessels being disturbed by the environment (such as wind, waves, and currents) and verified that the designed adaptive backstepping controller has good robustness to sea conditions through numerical simulation. Alamir et al. [26] proposed a nonlinear model predictive control method based on contraction theory and verified the convergence of the closed-loop system. Traditional DP control methods have shown poor adaptation to the wave direction and sea conditions [20], while the backstepping method has been shown to have strong robustness [25,27].

Due to the overactuated characteristics of the DP propulsion system, for horizontal lateral force, longitudinal force, and yaw moment control commands, there are multiple combinations of forces and thrust directions in the multiple thrusters. Therefore, optimization techniques are usually used to obtain the optimal solution to match the expected control commands generated by the DP controller, thereby ensuring the safe operation of the DP vessels. Many linear and nonlinear optimal thrust allocation methods for DP vessels have been proposed [28]. However, the constraints of the physical characteristics of the thrusters must be considered. Therefore, in engineering applications, control allocation is actually an optimization problem under constraint conditions [29]. The SQP method has been widely used in DP thrust allocation due to its simplicity and efficiency [30–33]. To avoid the reduction in the thrust efficiency due to the thruster–thruster and thruster–ship interference, most researchers reduced the problem of severe thrust loss by setting forbidden zones [30,34,35]. A small number of researchers have introduced an efficiency function to achieve azimuth thruster operation over 0–360 degrees with a modified SQP algorithm [36,37]. However, for azimuth thrusters and rudders, when using the SQP algorithm, Taylor expansion must be performed on the force and torque balance equations to construct the SQP solution form, and second-order and higher-order terms must be truncated. Therefore, the turning angle speed for azimuth thrusters or steering speed for rudders is strictly limited. The recommended value in the literature is generally 1 deg/s for full-scale ships [28], but the actual turning angle speed and rudder turning speed can reach 12 deg/s and 5 deg/s, respectively, making it difficult for azimuth thrusters and rudders to respond quickly to control commands and even posing a risk of reducing the thrust allocation accuracy. Therefore, to improve the accuracy of DP thrust allocation, the use of algorithms (for example, genetic algorithms [38] and particle swarm optimization (PSO) algorithms [39]) has been verified through numerical simulations. The firefly algorithm (FA), which was developed by Xin-She Yang at Cambridge University in 2007 [40], has a strong local search ability and can find the optimal solution in a small area [41]. This algorithm is easy to operate, is simple to implement, has fewer parameters, and there is less impact of parameters on the algorithm. However, due to the high dependence of the search method on excellent individuals, the convergence speed is reduced; therefore, to achieve engineering applications, we make some improvements to enhance the self-adaptive ability.

In view of the new concept of CTV engineering operation requirements, a DP ship synchronous following control strategy and a thrust allocation method are proposed, and relevant model experimental techniques are established. First, we took an FPSO unit as the leader vessel and a CTV as the follower vessel and proposed a synchronous following control strategy for a DP vessel based on virtual leader–follower and adaptive backstepping methods. Next, we achieved feedforward compensation of the external disturbance

caused by waves and the towing force, verified the global exponential convergence of the position and heading angle of the DP vessel based on contraction theory, and solved the nonuniversal parameter setting problem of the vessel DP system controller. A self-adaptive firefly (SAF) algorithm was proposed to optimize multiple thrusters considering forbidden zones in thrust allocation. Then, we embedded the control strategy in an independently developed DP control system, established a model experimental setup for a CTV synchronously following an FPSO unit while towing a tanker in irregular waves, and verified the effectiveness of the synchronous following control strategy proposed in this paper.

This article is organized as follows: Section 2 presents the virtual leader–follower strategy, low-frequency DP mathematical model, controller design, and contraction analysis. Section 3 describes the scaled model, experimental environment conditions, and test contents. Section 4 presents the experimental results of the scaled model, and the results are analyzed and discussed. Finally, conclusions are summarized and drawn in Section 5.

2. Mathematical Model and Methods

2.1. Virtual Leader–Follower Strategy

The dynamic positioning of a vessel DP only considers the motion of three degrees of freedom in the horizontal plane: surge, sway, and yaw. To better describe the motion of the DP vessel in the horizontal plane, we established Earth-fixed frame and Ship-fixed frame as the two coordinate frames of the leader vessel, virtual leader vessel, and follower vessel (as shown in Figure 2).

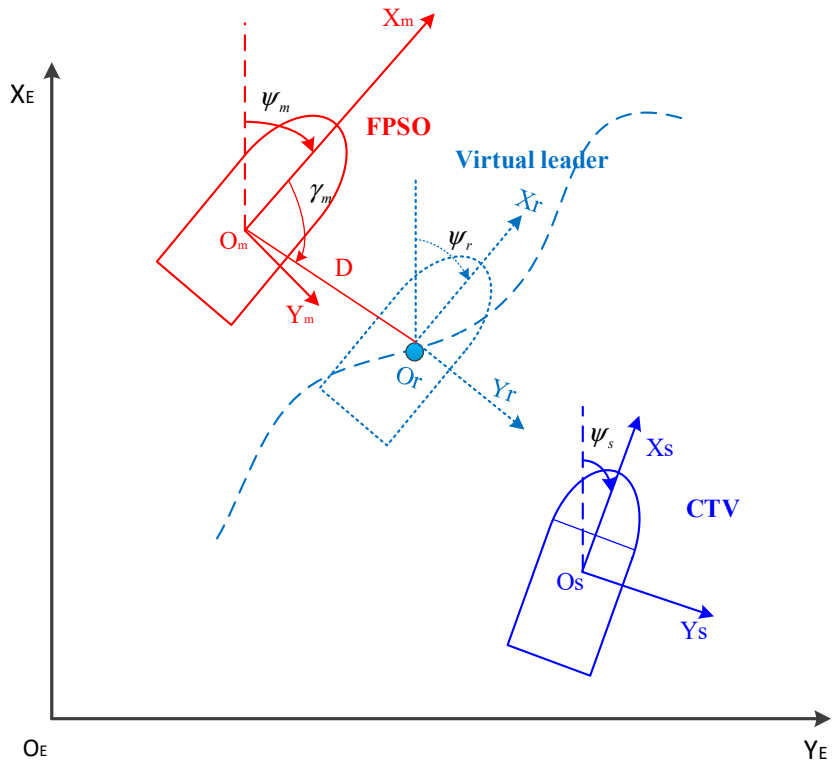

Figure 2. Schematic diagram of the virtual leader–follower strategy.

In Figure 2, $X_EO_EY_E$ is the Earth-fixed coordinate system, $X_mO_mY_m$ and $X_sO_sY_s$ are the Ship-fixed coordinate systems of the leader vessel and the follower vessel, respectively, and $X_rO_rY_r$ is the Ship-fixed coordinate system of the virtual leader vessel.

The tracking strategy based on the virtual leader–follower method (as shown in Figure 2) assumes a virtual FPSO unit as the leader, and the position of the virtual vessel relative to the leader is used as the feedback information of the closed-loop DP system. By designing the control strategy, the CTV and the FPSO unit maintain a certain target

distance D, and the virtual leader–follower method is adopted. The position and heading of the leader vessel and the virtual leader vessel should meet the following requirements:

$$\begin{aligned} \boldsymbol{\eta}_r &= \boldsymbol{\eta}_m + R(\psi_m)\boldsymbol{L} \\ R(\psi_m) &= \begin{bmatrix} \cos\psi_m & -\sin\psi_m & 0 \\ \sin\psi_m & \cos\psi_m & 0 \\ 0 & 0 & 1 \end{bmatrix} \end{aligned} \tag{1}$$

where $\boldsymbol{\eta}_m = [x_m, y_m, \psi_m]^{\mathrm{T}}$ represents the position and heading of the leader vessel, $\boldsymbol{\eta}_r = [x_r, y_r, \psi_r]^{\mathrm{T}}$ represents the position and heading of the virtual vessel, $R(\psi_m)$ is the transformation matrix between the Earth-fixed coordinate system and the Ship-fixed coordinate system, $L = [D\cos\gamma_m, D\sin\gamma_m, 0]^{\mathrm{T}}$, and γ_m is the angle between the longitudinal direction of the leader vessel and the line connecting the centers of gravity of the leader vessel and the virtual vessel.

Then, the speed relationship between the virtual vessel and the leader vessel is as follows [21]:

$$\begin{aligned} \dot{\boldsymbol{\eta}}_m &= R(\psi_m)\boldsymbol{v}_m \\ \dot{\boldsymbol{\eta}}_r &= \dot{\boldsymbol{\eta}}_m + R(\psi_m)S(r_m)\boldsymbol{L} + R(\psi_m)\dot{\boldsymbol{L}} \end{aligned} \tag{2}$$

where $\boldsymbol{v}_m = [u_m, v_m, r_m]^T$ and is composed of the longitudinal and lateral velocities and the heading angular velocity in the hull coordinate system of the leader vessel, and $S(r_m) = \begin{bmatrix} 0 & -r_m & 0 \\ r_m & 0 & 0 \\ 0 & 0 & 0 \end{bmatrix}$.

2.2. Mathematical Model

The CTV operates at low speed when synchronously following the FPSO unit with the DP system, so the nonlinear damping term is ignored, and its mathematical model can be expressed as [12]:

$$\begin{cases} \dot{\boldsymbol{\eta}}_s = R(\psi_s)\boldsymbol{v}_s \\ M\dot{\boldsymbol{v}}_s + D_L\boldsymbol{v}_s = \boldsymbol{\tau} + \boldsymbol{T}_{\mathrm{d}} \end{cases} \tag{3}$$

where $\boldsymbol{\eta}_s = [x_s, y_s, \psi_s]^{\mathrm{T}}$ is composed of the trajectory and heading angle of the follower vessel in the geodetic coordinate system; $\boldsymbol{v}_s = [u_s, v_s, r_s]^{\mathrm{T}}$ is composed of the surge, sway, and yaw angular velocities of the follower vessel in the hull coordinate system; $\boldsymbol{\tau} = [\tau_x, \tau_y, \tau_z]^{\mathrm{T}}$ is composed of the resultant force and moment under the action of waves and the towing force; $\boldsymbol{T}_{\mathrm{d}}$ is composed of the longitudinal and lateral control forces and the heading control moment generated by multiple thrusters; M is the inertia matrix with added mass ($M = M^T > 0$); and D_L is the linear damping matrix.

$$M = \begin{bmatrix} m - X_{\dot{u}} & 0 & 0 \\ 0 & m - Y_{\dot{v}} & -Y_{\dot{r}} \\ 0 & -N_{\dot{v}} & I_z - N_{\dot{r}} \end{bmatrix},\ D_L = -\begin{bmatrix} X_u & 0 & 0 \\ 0 & Y_v & Y_r \\ 0 & N_v & N_r \end{bmatrix} \tag{4}$$

where m is the mass of the vessel; I_z is the moment of inertia; $X_{\dot{u}}$, $Y_{\dot{v}}$ and $Y_{\dot{r}}$ are added masses; $N_{\dot{r}}$ is the added moment of inertia; X_u, Y_v, Y_r, and N_r are hydrodynamic derivatives.

2.3. Controller Design

Based on contraction theory, a backstepping control strategy for the DP vessel to synchronously follow the virtual leader vessel is designed. The main steps are as follows:

First, define the position and heading error between the follower vessel and the virtual vessel as

$$\boldsymbol{s}_1 = \boldsymbol{\eta}_s - \boldsymbol{\eta}_r \tag{5}$$

From Formula (5), the time derivative of $\boldsymbol{s}_1$ is obtained as

$$\dot{\boldsymbol{s}}_1 = R(\psi_s)\boldsymbol{v}_s - \dot{\boldsymbol{\eta}}_r = R(\psi_s)\boldsymbol{v}_s - (\dot{\boldsymbol{\eta}}_m + R(\psi_m)S(r_m)\boldsymbol{L} + R(\psi_m)\dot{\boldsymbol{L}}) \tag{6}$$

Let the speed vector $\boldsymbol{v}_s$ of the follower vessel be a virtual control quantity to design a virtual control function:

$$\boldsymbol{\alpha} = R^T(\psi_s)(-K_1\boldsymbol{s}_1 + \dot{\boldsymbol{\eta}}_r) \tag{7}$$

where $K_1 = \mathrm{diag}(k_{11}, k_{12}, k_{13}) > 0$ and is the design parameter matrix.

Define the speed error between the follower vessel and the virtual vessel as $\boldsymbol{s}_2 = \boldsymbol{v}_s - \alpha$. From Formulas (6) and (7), Formula (8) can be obtained:

$$\dot{\boldsymbol{s}}_1 = R(\psi_s)\boldsymbol{s}_2 - K_1\boldsymbol{s}_1 \tag{8}$$

Second, according to Formula (3), we can obtain the time derivative of $\boldsymbol{S}_2$:

$$\dot{\boldsymbol{s}}_2 = -M^{-1}D_L\boldsymbol{v}_s + M^{-1}\boldsymbol{\tau} + M^{-1}\boldsymbol{T}_\mathrm{d} - \dot{\boldsymbol{\alpha}} \tag{9}$$

Then, the synchronous following control law for the DP vessel is designed as follows:

$$\boldsymbol{\tau} = M[-K_2\boldsymbol{s}_2 + M^{-1}D_L\boldsymbol{v}_s - M^{-1}\hat{\boldsymbol{T}}_\mathrm{d} + \dot{\boldsymbol{\alpha}} - R^\mathrm{T}(\psi_s)\boldsymbol{s}_1] \tag{10}$$

where K_2 = diag(k_{21}, k_{22}, k_{23}) > 0 and $\hat{\boldsymbol{T}}_\mathrm{d}$ are the estimated vectors of the disturbance of the wave force and towing force, respectively. Then, Formula (11) can be obtained:

$$\dot{\boldsymbol{s}}_2 = -K_2\boldsymbol{s}_2 - R^T(\psi_s)\boldsymbol{s}_1 - M^{-1}(\hat{\boldsymbol{T}}_\mathrm{d} - \boldsymbol{T}_\mathrm{d}) \tag{11}$$

During actual operation, the interference of the DP vessel $\boldsymbol{T}_\mathrm{d}$ is bounded. To estimate the bounded interference $\boldsymbol{T}_\mathrm{d}$, the adaptive law is designed:

$$\dot{\hat{\boldsymbol{T}}}_\mathrm{d} = M\boldsymbol{s}_2 \tag{12}$$

Based on contraction theory, the virtual dynamic connection form of Formulas (8), (11) and (12) can be expressed as

$$\frac{d}{dt}\begin{pmatrix} \delta\boldsymbol{s}_1 \\ \delta\boldsymbol{s}_2 \\ \delta\hat{\boldsymbol{T}}_\mathrm{d} \end{pmatrix} = \begin{pmatrix} \boldsymbol{J}_{11} & \boldsymbol{J}_{12} \\ \boldsymbol{J}_{21} & 0 \end{pmatrix}\begin{pmatrix} \delta\boldsymbol{s}_1 \\ \delta\boldsymbol{s}_2 \\ \delta\hat{\boldsymbol{T}}_\mathrm{d} \end{pmatrix} \tag{13}$$

where the Jacobian matrix $\boldsymbol{J}_{11} = \begin{pmatrix} -\boldsymbol{K}_1 & R(\psi) \\ -R^T(\psi) & -\boldsymbol{K}_2 \end{pmatrix}$, and $\boldsymbol{J}_{21} = -\boldsymbol{J}_{12}^T = [\boldsymbol{0} \quad -\boldsymbol{M}^{-1}]$.

From the above formula, the matrix $\boldsymbol{J}_{11}$ is uniformly negative definite, and $\boldsymbol{M}^{-1}$ is smooth, so the error variables $\boldsymbol{s}_1$ and $\boldsymbol{s}_2$ globally and asymptotically converge to $\boldsymbol{0}$, and the estimated value of uncertain environmental disturbance is bounded.

Finally, from Formula (A5) in the Appendix A and Formulas (7) and (10), the virtual dynamic formula of the closed-loop control system can be obtained as

$$\frac{d}{dt}\begin{pmatrix} \delta\boldsymbol{\eta}_s \\ \delta\boldsymbol{v}_s \end{pmatrix} = \overline{J}\begin{pmatrix} \delta\boldsymbol{\eta}_s \\ \delta\boldsymbol{v}_s \end{pmatrix} \tag{14}$$

In the formula,

$$\bar{J} = \begin{bmatrix} \bar{J}_{11} & \bar{J}_{12} \\ \bar{J}_{21} & \bar{J}_{22} \end{bmatrix},$$

$$\bar{J}_{11} = \frac{\partial[R(\psi_s)v_s]}{\partial \eta_s^T},$$

$$\bar{J}_{12} = R(\psi_s),$$

$$\bar{J}_{21} = K_2 \frac{\partial \alpha}{\partial \eta_s^T} + \frac{\partial \dot{\alpha}}{\partial \eta_s^T} - \frac{\partial[R^T(\psi_s)(\eta_s - \eta_r)]}{\partial \eta_s^T}, \text{ and } \bar{J}_{22} = -K_2 - \frac{\partial \dot{\alpha}}{\partial \eta_s^T}.$$

If it can be proven that the Jacobian matrix $\bar{J} < 0$, then all solution trajectories of the closed-loop system exponentially converge to the desired trajectory, and the whole system is contracting.

According to the defined state error variable, the coordinate transformation can be obtained as

$$\begin{bmatrix} \delta s_1 \\ \delta s_2 \end{bmatrix} = \Theta \begin{bmatrix} \delta \eta_s \\ \delta v_s \end{bmatrix} \tag{15}$$

In the formula, δs_1 and $\delta \eta_s$ are the virtual displacements, δs_2 and δv_s are the virtual velocities, and the invertible matrix Θ is

$$\Theta = \begin{pmatrix} \mathrm{I}_{3\times 3} & 0 \\ -\partial \alpha / \partial \eta_s^T & \mathrm{I}_{3\times 3} \end{pmatrix} \tag{16}$$

The transformation matrix $\mathrm{P} = \Theta^T \Theta$ is

$$\mathrm{P} = \begin{bmatrix} \mathrm{I}_{3\times 3} + [\frac{\partial \alpha}{\partial \eta_s}]^T \frac{\partial \alpha}{\partial \eta_s} & -[\frac{\partial \alpha}{\partial \eta_s}]^T \\ -\frac{\partial \alpha}{\partial \eta_s} & \mathrm{I}_{3\times 3} \end{bmatrix} \tag{17}$$

Formula (7) indicates that by selecting a reasonable value for the controller parameter K_1, the transformation matrix P is guaranteed to be positive definite.

From Formulas (14) and (17), we obtain

$$\frac{d}{dt} \begin{pmatrix} \delta s_1 \\ \delta s_2 \end{pmatrix} = \widetilde{J} \begin{pmatrix} \delta s_1 \\ \delta s_2 \end{pmatrix} \tag{18}$$

where the Jacobian matrix $\widetilde{J} = (\dot{\Theta} + \Theta \bar{J}) \Theta^{-1} = \begin{bmatrix} \widetilde{J}_{11} & \widetilde{J}_{12} \\ \widetilde{J}_{21} & \widetilde{J}_{22} \end{bmatrix}$.

Formula (13) indicates that the error system composed of Formulas (8) and (11) is contracting; that is, if the Jacobian matrix $\widetilde{J}$ is uniformly negative definite, then all the solutions of the original closed-loop system exponentially converge to a certain trajectory, and the system is contracting, thus ensuring that the position and heading angle of the follower vessel globally exponentially converge to and remain on those of the virtual vessel η_s.

2.4. Thrust Allocation

The thrust allocation algorithm should be optimized for lower power consumption and wear and tear of the thruster devices. To ensure safe operation, the ability of thrust allocation to always generalize an optimal solution in time is very important, and can be taken as an optimization problem with cost functions and constraints.

The cost functions can be formulated as follows [15].

$$J(\alpha, f, s) = \sum_{i=1}^{m} (f^{\mathrm{T}} P f + (f - f_0)^{\mathrm{T}} M (f - f_0) + (\alpha - \alpha_0)^{\mathrm{T}} Q (\alpha - \alpha_0) + s^{\mathrm{T}} W s) \quad (19)$$

where P is a diagonal matrix, $f \in R^n$ is a vector of thruster forces, $\alpha \in R^n$ is a vector of azimuth angles at sample time k, f_0 and α_0 are the force and angle at time $k-1$, respectively, and $s \in R^3$ is a vector of slack variables introduced to ensure the existence of a solution. $M \in R^{n \times n}$ and $Q \in R^{n \times n}$ are weighting matrices, and the matrix $W \in R^{3 \times 3}$ is significantly larger to force the optimal solution $s \approx 0$.

The equality constraint is most important to ensure that the controlled forces and moments are produced:

$$s + B(\alpha) f = T \quad (20)$$

where B is the thruster configuration matrix, $T = [F_{\mathrm{x}}, F_{\mathrm{y}}, M_{\mathrm{z}}]^{\mathrm{T}}$, F_{x} is the surge force, F_{y} is the sway force, and M_{z} is the moment in the yaw direction.

Assuming that there are n_f tunnel thrusters and n_p azimuth thrusters and that each thruster k is located at (x_i, y_i), the thruster configuration matrix can be expressed as follows:

$$\mathrm{B}(\alpha_{i=1:n_f}) = \begin{pmatrix} 0 \\ 1 \\ -y_i \cdot \cos\alpha_i + x_i \cdot \sin\alpha_i \end{pmatrix}, \mathrm{B}(\alpha_{i=n_f+1:n_f+n_p}) = \begin{pmatrix} \cos\alpha_i \\ \sin\alpha_i \\ -y_i \cdot \cos\alpha_i + x_i \cdot \sin\alpha_i \end{pmatrix} \quad (21)$$

The physical constraints on the power limitation, saturation of the RPM input, and turning rate of the azimuth angle can be expressed as follows:

$$\begin{aligned} & \mathrm{f}_{\min} - \mathrm{f}_0 \le \Delta \mathrm{f} \le \mathrm{f}_{\max} - \mathrm{f}_0 \\ & \Delta \mathrm{f}_{\min} \le \Delta \mathrm{f} \le \Delta \mathrm{f}_{\max} \\ & \alpha_{\min} - \alpha_0 \le \Delta\alpha \le \alpha_{\max} - \alpha_0 \\ & \Delta\alpha_{\min} \le \Delta\alpha \le \Delta\alpha_{\max} \\ & s_{x\min} \le s_x \le s_{x\max} \\ & s_{y\min} \le s_y \le s_{y\max} \\ & s_{y\min} \le s_z \le s_{z\max} \end{aligned} \quad (22)$$

where $\mathrm{f}_{\max} \in R^n$ is a vector of maximum thrust, $\mathrm{f}_{\min} \in R^n$ is a vector of minimum thrust, and the maximum $\Delta \mathrm{f}_{\max} \in R^n$ and minimum $\Delta \mathrm{f}_{\min} \in R^n$ are the rates of change of thrust. The maximum $\Delta\alpha_{\max} \in R^n$ and minimum $\Delta\alpha_{\min} \in R^n$ are the rates of change in the thrust direction; s_i (i = x, y and z) denotes the slack variable.

In this paper, the above formulated optimization problem can be solved by the FA, which was proposed by Yang for solving optimization problems [40].

In the FA, the brightness and attractiveness are two main parameters; brightness guides the direction of fireflies and attractiveness indicates the forward momentum of fireflies with low brightness. Since the brightness of fireflies gradually weakens with distance, absolute and relative brightness are used for characterization.

For any two fireflies i and j in the group, the I_{i} represents the brightness of ith firefly. The relative brightness I_{ij} can be expressed as follows:

$$\begin{aligned} & I_{ij}(r_{ij}) = I_i e^{-\gamma r_{ij}^2} \\ & r_{ij} = \left\| \mathrm{x}_i - \mathrm{x}_j \right\| = \sqrt{\sum_{k=1}^{D} (x_{i,k} - x_{j,k})^2} \end{aligned} \quad (23)$$

where γ is light absorption coefficient, r_{ij} is the distance between firefly i and firefly j, D is spatial location dimension, $x_{i,k}$ is the kth component of the spatial location x_i of ith firefly.

The firefly's attractiveness is defined as follows:

$$\beta_{ij}(r_{ij}) = \beta_0 e^{-\gamma r_{ij}^2} \tag{24}$$

where β_0 is attractiveness at $r_{ij} = 0$.

The firefly i will be attracted to another more brighter firefly j, and the spatial location x_i is defined as:

$$x_i^{N_{iteration}+1}(t) = x_i^{N_{iteration}}(t) + \beta_{ij} \times (x_j^{N_{iteration}}(t) - x_i^{N_{iteration}}(t)) + \alpha \times (rand - 1/2) \tag{25}$$

where t is the sampling time, $N_{iteration}$ is the number of generations, and x_i and x_j are the firefly i and j positions in the D-dimensional space, respectively, α is the step size factor, and rand is a uniformly distributed random number.

To reduce the complexity of the FA and avoid the generation of local optimal solutions, the N^{th} generation of the FA with strong brightness at spatial position x is selected to attract the movement of other fireflies. While ensuring that the firefly search process is affected by the spatial distance, the attraction model is improved to make the search direction more reasonable. The improved attraction model is as follows:

$$\begin{aligned} \beta_{ij}(r_{ij}) &= \theta \cdot \beta_0 e^{-\gamma r_{ij}^2} \\ \theta &= 1 - \frac{N_{iteration}}{N_{\max}} \end{aligned} \tag{26}$$

where $N_{\max}$ is the maximum number of generations.

In the position update formula of the standard FA, the constant step factor a will not be conducive to the convergence of the optimal solution of the population. Therefore, to improve the convergence of the FA, an adaptive step size factor that varies with the number of iterations is adopted, and its expression is as follows:

$$\alpha_{N_{iteration}} = \alpha_0 (1 - e^{-(1 - \frac{N_{iteration}}{N_{\max}})}) \tag{27}$$

The pseudocode of the thrust allocation-based SAF algorithm is shown in Algorithm 1.

Algorithm 1 SAF algorithm

Inputs:
Maximum number of iterations $N_{\max}$;
The population number N_{pop};
The cost functions $f(x) = \min\{J(\alpha, f, s)\}, x = [f_1, f_2, \ldots, f_n, \alpha_1, \alpha_2, \ldots \alpha_n,]^T$
Initial boundary limits L_b and U_b; the dimension D, which is twice the number of thrusters.
Initial $x = L_b + (U_b - L_b) \times \text{rand}(D,1)$
Initialize parameters α_0, β_0, γ
Initialize firefly population x_i (i = 1, 2, …, Npop), number of fireflies.
Calculate the f(x), optimal solution x_{Gbest} is determined for initialize firefly population
While ($N_{\text{iteration}} << N_{\max}$)
    for i = 1: N_{pop}
        calculate the distance $r_{i,Gbest} = \|x_i - x_{Gbest}\| = \sqrt{\sum_{k=1}^{D} (x_{i,k} - x_{\text{Gbest},k})^2}$
        update the position x_i by Equations (25)–(27)
        boundary treatment $x_i \in [x_{i,L_b}, x_{i,U_b}]$ x_{i,L_b}, x_{i,U_b} are the upper and lower bounds
    end
        obtain a new $x_i^{N_{iteration}+1}(t)$
end while
Outputs: the optimal solution $x_{Gbest}(t)$

3. Test Overview

3.1. Test Objects

The test object is an 8000-ton CTV. By comprehensively considering the tank testing and wave-making capacity, the installation and arrangement requirements of the model thruster, and the adjustment of the center of gravity and inertia of the test model, the scale ratio of the model is taken as 1:22. The main parameters of the CTV, FPSO unit, and tanker are shown in Table 1. Restricted by the main scale of the basin, the actual scale ratio of the FPSO unit model is 1:68.

Table 1. Model particulars of the CTV, FPSO unit, and tanker.

Parameter	Symbol	Unit	FPSO Model	Tanker	CTV	
					Full-Scale	Model
Length Overall	L_{OA}	m	4.1590	6.8158	89.00	4.0455
Breadth	B	m	0.6820	1.1461	20.00	0.9091
Depth	D	m	0.3320	0.5394	10.50	0.4773
Displacement	△	t	0.2270	1.3511	8030	0.7357
Mean draft	T	m	0.1310	0.2994	6.50	0.2955

The CTV is equipped with four azimuth thrusters and one tunnel thruster at the bottom of the bow. The thrusters are simulated according to geometric similarity and power similarity. The main parameters are shown in Table 2. The thruster numbers and layout are shown in Figure 3.

Table 2. Main parameters of the thrusters (scale ratio is 1:22).

Parameter	Unit	T1&T2		T3&T4		T5	
		Full-Scale	Model	Full-Scale	Model	Full-Scale	Model
Thrust	kN	745.56	0.0700	345.312	0.0324	107.91	0.0101
Diameter	m	3.900	0.1636	2.600	0.1182	1.700	0.0773
Thrust from 0 to T_{max}	kN/s	33.0	0.1454	23.0	0.0101	10.80	0.0048
Azimuth angle from 0 deg to 180 deg	deg/s	12	56.28	12	56.28	/	/

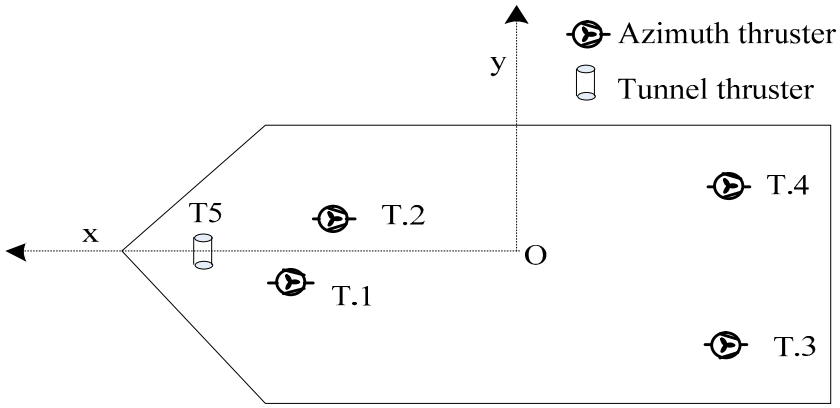

Figure 3. Schematic diagram of the thruster number and layout.

Before the DP model experiment, thruster-hull and thruster-thruster interaction tests were carried out. The thrust forbidden zones are set to [−60°, 30°], [110°, 150°], [200°, 290°] and [70°, 170°], corresponding to thrusters 1, 2, 3 and 4, respectively.

3.2. Simulation of the Flexible Link System with Multiple Floating Bodies

3.2.1. Simulation of the Mooring System of the FPSO Unit

Because the scale ratio of the FPSO unit is different from those of the tanker and the CTV, the stiffness of the mooring system of the FPSO unit cannot be determined according to the scale ratio. Therefore, this test does not simulate the mooring system of the FPSO unit and only simulates the statistical characteristics of the motion of the FPSO unit.

3.2.2. Simulation of the Mooring System of the Tanker

The tanker is connected to the CTV through two mooring cables, which are each composed of a 150 m-long nylon rope and a 9 m-long iron chain. The cables are simulated according to diameter similarity, weight similarity, and stiffness similarity.

3.3. Test Environment Conditions and Contents

The JONSWAP spectrum is adopted in the model test to simulate an irregular wave environment. The JONSWAP spectral density is defined as follows:

$$S_\zeta(\omega) = \alpha H_{1/3}^2 \omega_P^4 \omega^{-5} \exp\left\{-1.25(\omega/\omega_P)^{-4}\right\} \times \gamma^{\exp\left\{-\left(\frac{\omega/\omega_P-1}{\sqrt{2}\sigma}\right)^2\right\}} \quad (28)$$

where $H_{1/3}$ is the significant wave height, ω_p is the spectrum peak frequency, ω is the circular wave frequency, and γ is the peak enhancement factor (for this test, γ = 2.2). When $\omega < \omega_p$, σ is 0.07, and when $\omega > \omega_p$, σ is 0.09; $\alpha = \frac{0.0624}{0.230+0.0336\gamma-0.185/(1.9+\gamma)}$.

The headings against waves are defined as follows: The wave coming from the bow is defined as 180° (head sea), and that coming from the starboard is defined as 90° (beam sea). The significant wave height and spectral peak period combinations are listed in Table 3.

Table 3. Test contents for synchronous following control of the CTV in the towing state.

Test No.	Wave Heading (°)	$H_{1/3}$		T_p		γ
		Full-Scale (m)	Model (mm)	Full-Scale (s)	Model (s)	
F01 F02	180 135	2.00	90.91	9.21	1.964	2

Irregular waves are generated by an L-type shaking plate wave generator with approximately 200 oscillating flaps.

Before the experiments, the JONSWAP spectrum of irregular waves was calibrated, and the calibrated results (model scale) are shown in Figure 4. The significant wave height ($H_{1/3}$) and spectral peak period (T_p) are within 5% of the theoretical values under the two headings against waves.

3.4. Test Setup

The scaled experiments are carried out in the seakeeping basin of China Ship Scientific Research Center (CSSRC) with dimensions of 69 m × 46 m × 4 m (length × width × water depth). The initial state of the test is set as the longitudinal tandem mode of the FPSO unit, the CTV, and the tanker. According to the CTV operation requirements, the distance between the stern end of the FPSO unit and the bow end of the CTV should be 4.545 m (corresponding to 100 m at full scale), the distance between the stern end of the CTV and the bow end of the tanker should be 6.818 m (corresponding to at full scale), and the heading angles of the three vessels should all be 0°. A schematic diagram and photographs of the tank layout are shown in Figures 5 and 6, respectively.

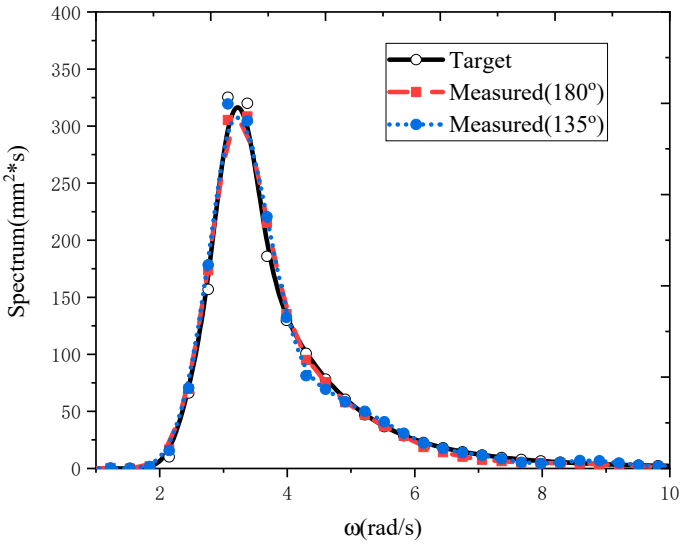

Figure 4. Calibrated wave spectrum.

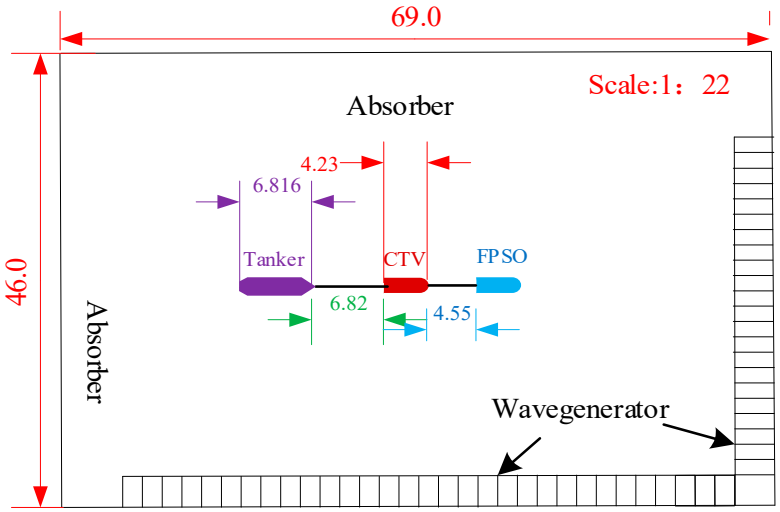

Figure 5. Schematic diagram of the FPSO unit, CTV, and tanker layout.

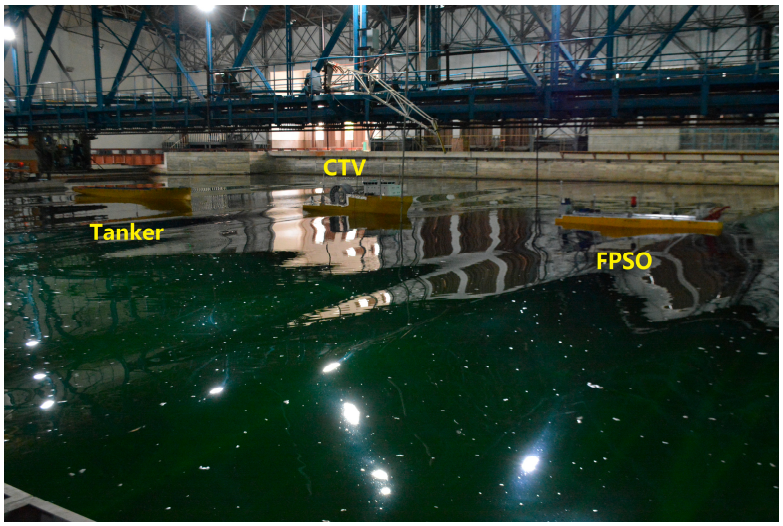

Figure 6. Photographs of the FPSO unit, CTV, and tanker in the experiment.

4. Experimental Results and Analysis

In the experimental verification, all the results are transformed to full-scale according to Froude number similarity. The added mass and added moment of inertia in the inertia matrix M and the linear damping matrix D_L are obtained by numerical calculation:

$$M = \begin{vmatrix} 8.68907 \times 10^5 & 0 & 0 \\ 0 & 1.44489 \times 10^7 & 0 \\ 0 & 0 & 5.74462 \times 10^9 \end{vmatrix}, \; D_L = \begin{vmatrix} 5.19397 \times 10^3 & 0 & 0 \\ 0 & 3.26129 \times 10^4 & -8.94123 \times 10^3 \\ 0 & 5.98832 \times 10^5 & 1.38939 \times 10^7 \end{vmatrix}$$

4.1. Simulation of the Motion Characteristics of the FPSO Unit

To ensure the successful simulation of the statistical characteristics of the FPSO unit motion, a multifloating body model mooring test was carried out before this test (the scale ratios of the FPSO unit, the CTV, and the tanker were all 1:80). The CTV counteracts the influence of second-order wave forces through horizontal mooring during the model experiment. The statistical results of the sway, surge, and yaw motions of the FPSO unit in the multifloating body model mooring test and the synchronous following test with the DP system are shown in Table 4. As can be seen from Table 4, the motion results of the FPSO unit in this test are slightly larger; Figure 7 shows the time history curves of FPSO for acceleration in the x and y directions and the angular velocity of the heading. Figure 7a,c show the results of the synchronous following control test in the wave headings 0° and 135°, respectively. Figure 7b,d show the multifloating body model mooring test in the wave headings 0° and 135°, respectively. As can be seen from Figure 7, the acceleration and angular velocity of FPSO are obviously larger during the synchronous following test, so the results can more effectively verify the ability of the designed synchronous following control strategy to maintain a safe operating distance between the FPSO unit and the CTV.

Table 4. Statistical motion results of the FPSO unit under the horizontal mooring system.

Test No.	Wave Heading (°)	Item	FPSO (CTV with Mooring)			FPSO (CTV with DP System)		
			Surge (m)	Sway (m)	Yaw (°)	Surge (m)	Sway (m)	Yaw (°)
F01	180	Max	0.815	0.342	0.05	2.442	0.528	1.863
		Min	−1.145	−0.798	−0.206	−1.254	−0.418	−1.147
		Mean	−0.008	0.002	−0.069	0.523	0.065	0.361
		SD	0.543	0.072	0.035	0.710	0.155	0.386
F02	135	Max	2.529	−2.352	0.783	−2.064	−2.184	2.434
		Min	−4.983	−4.314	1.459	−6.533	−5.982	−2.451
		Mean	−1.481	−3.238	0.035	−4.268	−4.025	−0.133
		SD	1.129	0.303	0.268	0.780	0.623	0.700

4.2. Analysis of the Capability of the CTV to Synchronously follow the FPSO Unit

Table 5 shows the statistical values of the sway, surge, and yaw motions of the CTV under different wave heading conditions. All the results in the table are converted into the full-scale vessel state, and the time–history curves of the CTV motion trajectories and heading errors corresponding to different wave heading conditions are shown in Figures 8 and 9.

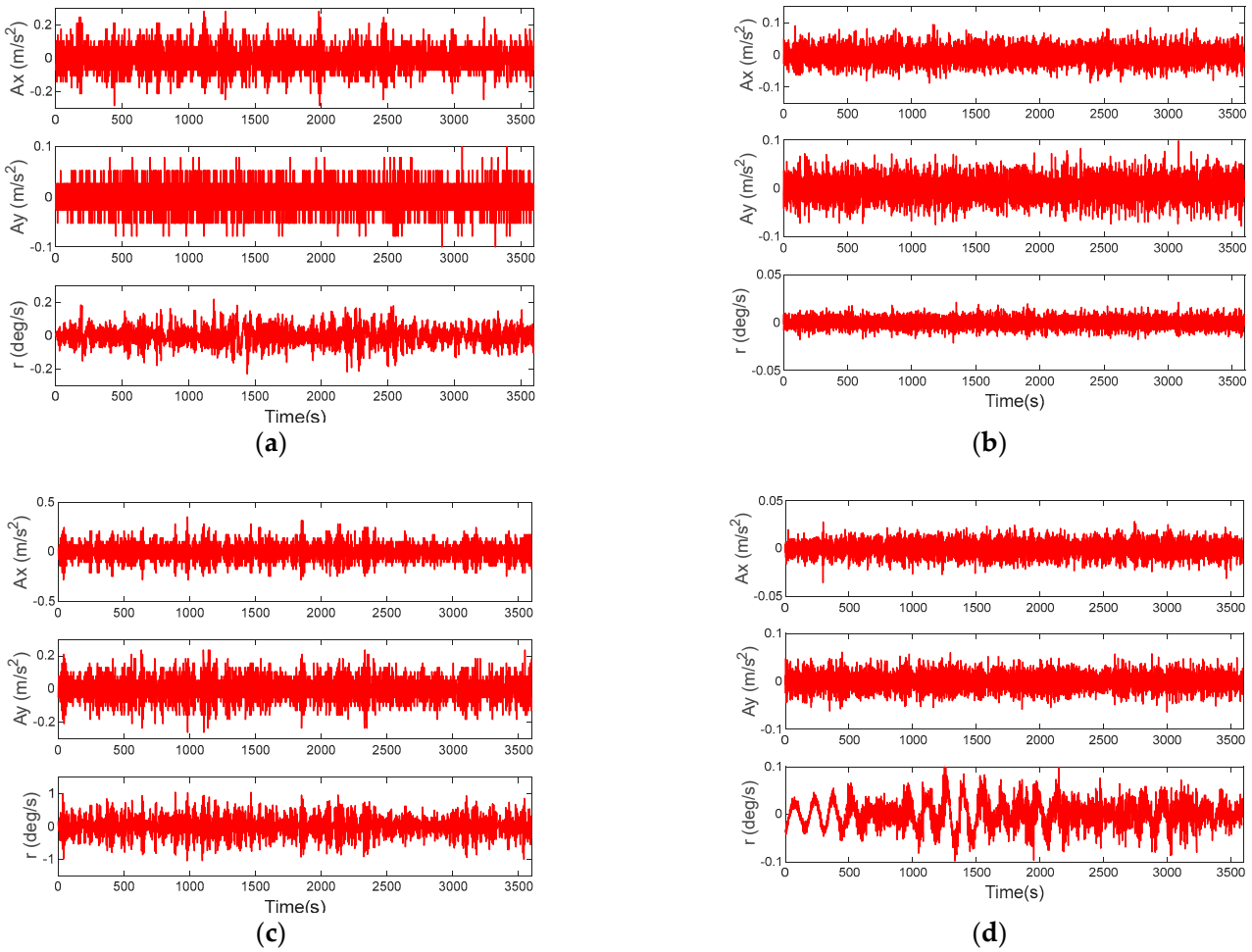

Figure 7. Time–history curves of the FPSO acceleration: (**a**) DP test in wave heading 180°; (**b**) mooring test in wave heading is 180°; (**c**) DP test in wave heading 135°; (**d**) mooring test in wave heading 135°.

Table 5. Statistical results of the motion of the CTV synchronously following the FPSO unit.

Test No.	Wave Heading	Motion	Unit	Mean	Min	Max	Error
F01	180°	Yaw	deg	−0.55	−2.63	2.15	1.65
		Surge	m	−1.52	−3.23	0.29	/
		Sway	m	0.89	−3.28	4.86	/
F02	135°	Yaw	deg	1.28	−5.89	1.04	2.45
		Surge	m	−3.26	−14.70	7.50	/
		Sway	m	−0.72	−13.44	8.68	/

The results in Table 5 show that when the wave heading is 180°, the control effects for surge and sway of the CTV are equivalent, and the average error of the heading control is only −0.55°. At 1400 s and 3400 s in the test (as shown in Figure 9a), the lateral tracking error of the CTV is slightly larger since the CTV is towing the tanker, which leads to a greater deviation in the heading. At this time, the maximum heading error of the CTV following the FPSO unit is 1.65°. When the wave heading is 135°, the capability of the CTV to synchronously follow the position and heading of the FPSO unit is slightly reduced, but the synchronous following error of the heading is still controlled within 2.45°, which effectively verifies that the control strategy in this paper can achieve a synchronous following response

of the heading motion and confirms the robustness of the control strategy to different wave heading conditions.

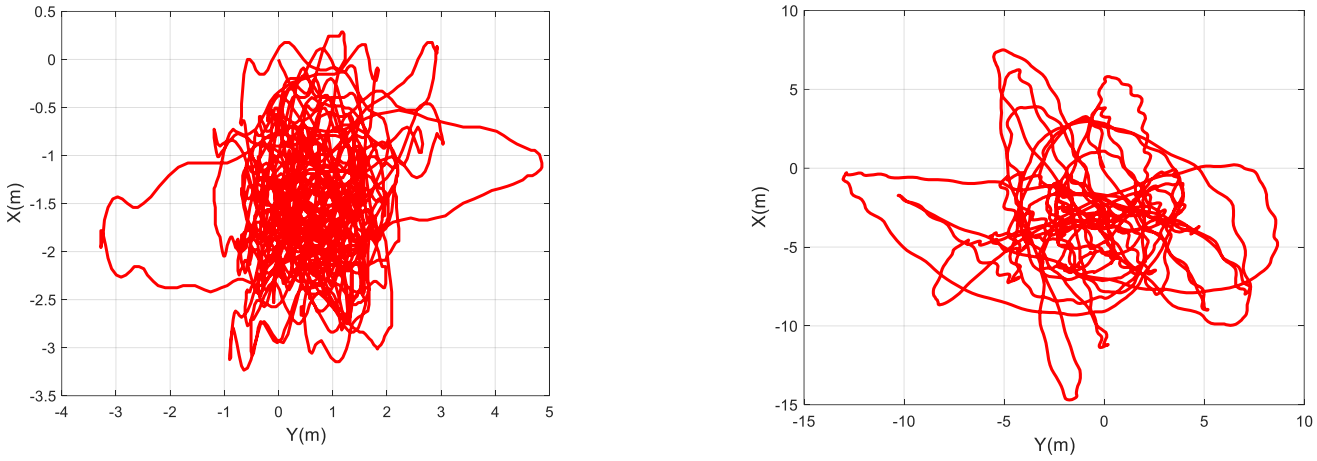

(**a**) (**b**)

Figure 8. Time–history curves of the CTV trajectory: (**a**) wave heading is 180°; (**b**) wave heading is 135°.

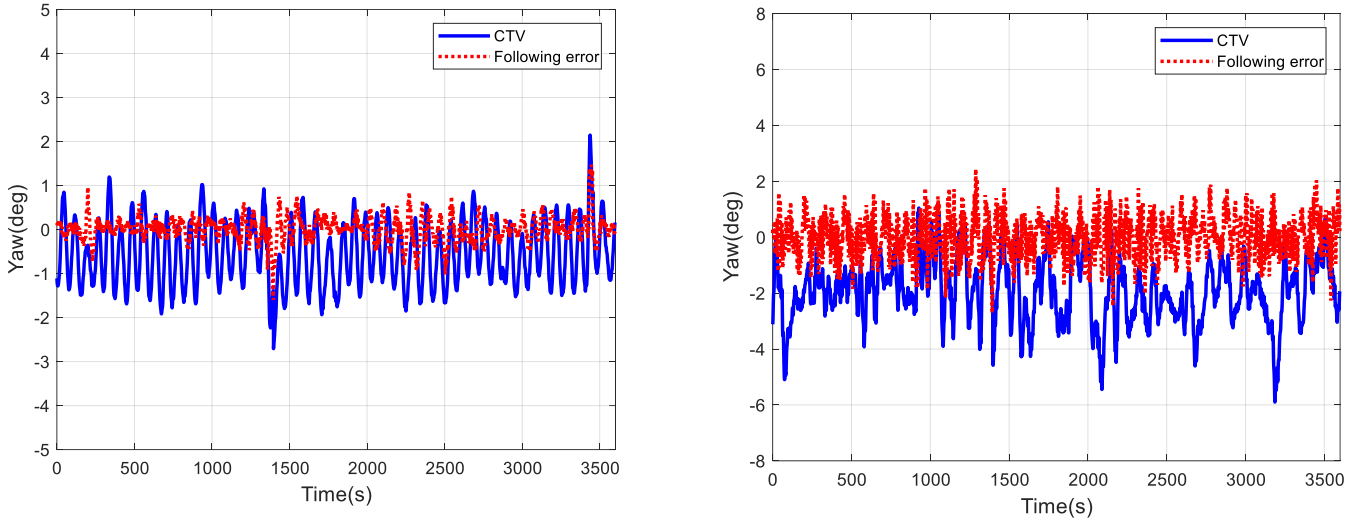

(**a**) (**b**)

Figure 9. Time–history curves of the heading tracking error of the CTV: (**a**) wave heading is 180°; (**b**) wave heading is 135°.

Figure 10 shows the time–history curves of the distance between the CTV and the FPSO unit under two wave heading conditions, 180° and 135°. As observed in the figure, when the wave heading is 180°, the CTV and the FPSO unit can effectively maintain a safe distance of 100 m with a maximum deviation of 3.78 m and an average deviation of only 0.99 m (95% CI = [0.96, 1.03]); when the wave heading is 135°, due to the reduced heading control accuracy, the distance between the CTV and the FPSO unit is slightly larger, with a maximum deviation of 14.38 m and an average deviation of 2.53 m (95% CI = [2.42, 2.64]), which effectively verifies that the control strategy proposed in this paper can achieve safe and cooperative operation between the CTV and the FPSO unit.

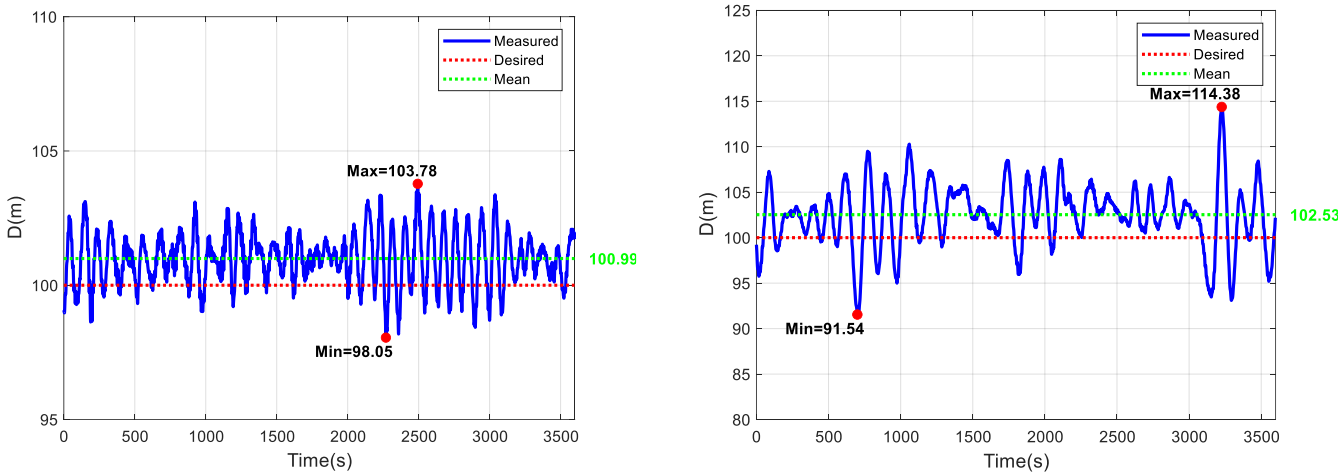

(**a**) (**b**)

Figure 10. Time–history curves of the distance between the CTV and the FPSO unit: (**a**) wave heading is 180°; (**b**) wave heading is 135°.

To verify the advantages of the SAF algorithm, the SQP algorithm and PSO algorithm are used to compare the experimental results. When using the SQP algorithm, to reduce the truncation error of second-order and higher-order terms produced by Taylor expansions, the rotation speed of the azimuth thruster is selected as 1 deg/s (corresponding to full scale), whereas the rotation speed for the corresponding PSO algorithm is similar to that for the SAF algorithm, which is 12 deg/s (corresponding to full scale).

In order to demonstrate how the firefly algorithm works, consider the maximum number of iterations $N_{\max}$ = 150, the population number N_{pop} = 60, and initialization parameters $\alpha_0 = 1$, $\beta_0 = 1$, $\gamma = 0.1$. Figure 11 shows the comparison results of the longitudinal, transverse, and heading thrust allocation commands and control commands for the three degrees of freedom in the horizontal plane under the 180° wave heading. Due to the principle of heading control priority (slack variable matrix W = diag [10^3,10^3,10^4]), the thrust allocation priority satisfies the heading moment control command. The optimal solution of the yaw moment is almost identical to the control command, and due to the small environmental force under the wave heading of 180°, the lateral and longitudinal control forces are also in good agreement with the control command. Figure 12 shows the comparison results of thrust allocation when the wave heading is 135°. Under this condition, the wave force acting on the CTV in the lateral and yaw directions significantly increases, and its sway, surge, and yaw motions also significantly increase, resulting in a larger error between CTV thrust allocation commands and control commands. However, the optimal solution and control commands for the yaw moment are still better than those in the lateral and longitudinal directions.

To test the effectiveness of the proposed thrust allocation algorithm, R-squared (R^2) is introduced to evaluate the accuracy of the actual thrusts and control commands.

$$R^2 = 1 - \frac{\sum_{i=1}^{N} \left(x\_command(i) - x\_allocation(i)\right)^2}{\sum_{i=1}^{N} \left(x\_command(i) - \hat{x}(i)\right)^2} \tag{29}$$

where $x\_command(i)$ and $x\_allocation(i)$ denote the control command and actual allocation result, respectively, and $\hat{x}(i)$ represents the average of the control commands. When the allocation values perfectly match the control commands, R^2 is 1.

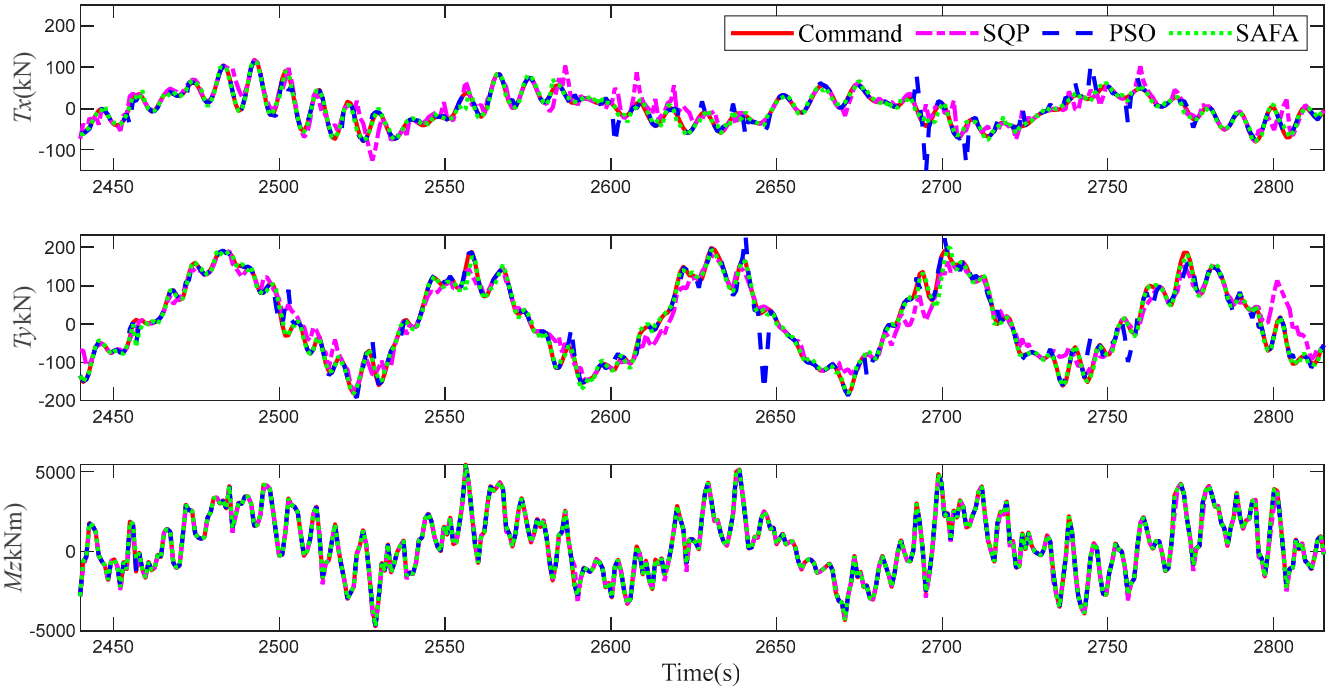

Figure 11. Time–history curves of the control command and thrust allocation under a 180° wave heading.

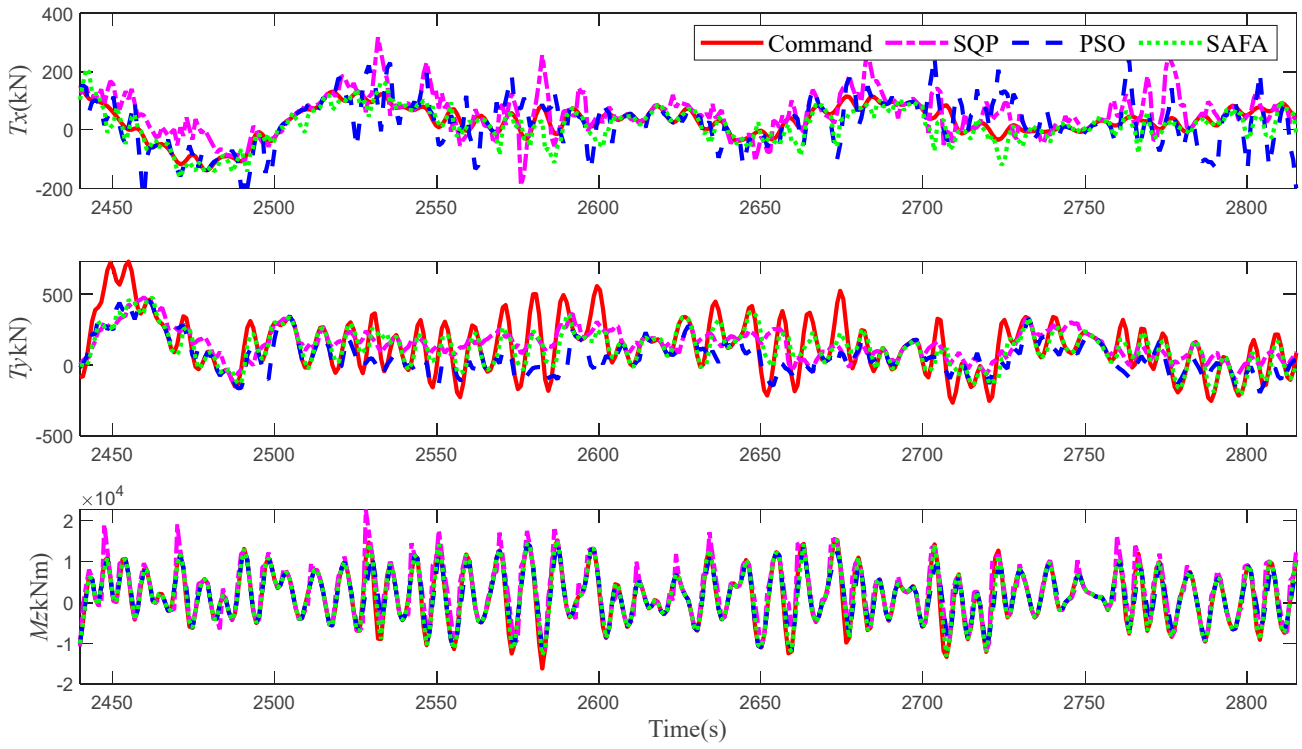

Figure 12. Time–history curves of the control command and thrust allocation under a 135° wave heading.

Figures 13 and 14 show the accuracy and total power consumption comparisons between the SAF algorithm proposed in this paper, the SQP algorithm and the PSO algorithm. According to Figure 13a, when the wave heading is 180°, the actual optimal torque command issued by the propulsion system is almost identical to the control command for the three algorithms, with R^2 values of 0.9727 (SQP), 0.9993 (PSO), and 0.9996 (SAF). The SAF algorithm outperforms the SQP and PSO algorithms in longitudinal and lateral forces. However, compared to the SAF algorithm and PSO algorithm, the SQP algorithm is

limited by a rotation angle speed of only 1 deg/s, resulting in a large error in lateral and longitudinal forces. From Figure 13b, the proposed SAF algorithm has higher accuracy under a 180° wave heading, while the power consumption is lower than that for the PSO algorithm. The reason for the lower power consumption of the SQP algorithm is that the smaller force and moment errors result in the first term of Equation (19) being smaller. When the wave heading is 135°, from Figure 8b, Figure 9b, and Figure 12, the wave force and coupled motion significantly increase. Due to the principle of prioritizing heading control, the three allocation algorithms can still meet the control requirements for the yaw torque, and the SQP algorithm even has a slightly higher accuracy in yaw control allocation than the PSO and SAF algorithms, with R^2 values of 0.9876 (SQP), 0.9087 (PSO), and 0.9694 (SAF). However, the accuracy of the SQP algorithm is significantly decreased for lateral and longitudinal forces because the SQP algorithm can only achieve the optimal solution by quickly adjusting the thrust, and the power significantly increases compared to the PSO and SAF algorithms due to the strict limitation of the lower rotation angle speed.

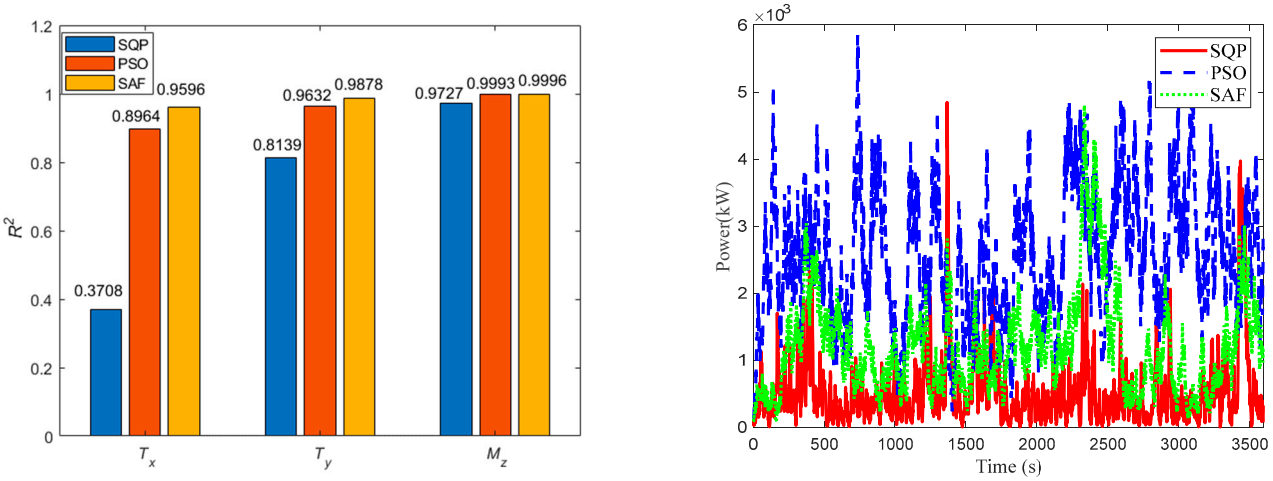

(**a**) (**b**)

Figure 13. R^2 and total power comparison of different thrust allocation algorithms under a 180° wave heading: (**a**) R^2; (**b**) total power comparison.

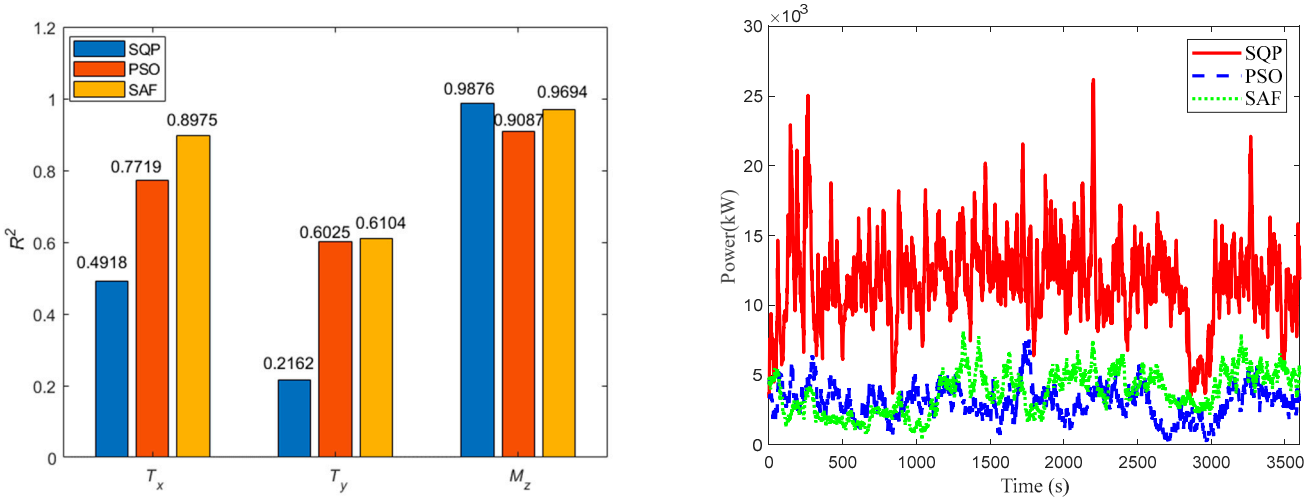

(**a**) (**b**)

Figure 14. R^2 and total power comparison of different thrust allocation algorithms under a 135° wave heading: (**a**) R^2; (**b**) total power comparison.

From Figures 13b and 14b, we can see that due to limitations of the SQP algorithm for azimuth thrusters in thrust allocation and the different rotation angle speeds, comparing the power consumption of the SQP, PSO, and SAF algorithms is no longer meaningful. Table 6 shows the total power consumption of the CTV. From Table 6, when the wave heading is 180°, compared with the PSO algorithm, the SAF algorithm has lower maximum and average power consumption. When the wave direction is 135°, due to the intensification of coupled motion, to satisfy the yaw moment, the higher thrust allocation accuracy leads to smaller relaxation variable errors. Although the SAF algorithm has higher accuracy, this causes an increase in power compared to the PSO algorithm, with the maximum and average power increased by 8.53% and 7.80%, respectively. Actually, the first and fourth terms in Equation (19) are inherently contradictory, and the allocation accuracy and power consumption trade-off can be solved by adjusting the matrix weight.

Table 6. Statistical results of power consumption for all thrusters of the CTV.

Wave Heading	Control Allocation	Power (kW)			
		Max	Mean	SD	95% Confidence Interval on Mean
180°	PSO	5850	2557	989	[2526, 2588]
	SAF	4802	1193	734	[1170, 1216]
135°	PSO	7541	3526	1155	[3490, 3562]
	SAF	8184	3801	1489	[3755, 3847]

Tables 7 and 8 show the statistical occurrence results for the power utilization of all thrusters under the two wave heading conditions. The results in Tables 7 and 8 show that when the wave heading is 180°, except for thrusters 1 and 2, the power utilization rate of each thruster is basically within 20%; when the wave heading is 135°, due to the increases in the control force, moment, and allocation accuracy, the power utilization (>40%) of all thrusters significantly increases with the SAF algorithm compared to the PSO algorithm.

Table 7. Occurrence of power utilization for each thruster of the CTV under a wave heading of 180°.

Power Utilization	Thrust Allocation	Occurrence (%)				
		No. 1	No. 2	No. 3	No. 4	No. 5
0~20%	PSO	4.72	14.81	90.04	99.95	96.61
	SAF	28.83	52.97	92.18	100.00	89.44
20~40%	PSO	17.41	20.72	8.84	0.05	1.75
	SAF	40.80	33.45	6.67	0.00	5.81
40~60%	PSO	28.55	22.31	1.12	0.00	0.70
	SAF	21.19	9.15	1.15	0.00	2.66
60~80%	PSO	25.31	24.56	0.00	0.00	0.47
	SAF	7.48	2.27	0.00	0.00	1.07
80~100%	PSO	24.01	17.596	0	0	15.98
	SAF	1.69	2.164	0	0	5.18

Table 8. Occurrence of power utilization for each thruster of the CTV under a wave heading of 135°.

Power Utilization	Thrust Allocation	Occurrence (%)				
		No. 1	**No. 2**	**No. 3**	**No. 4**	**No. 5**
0~20%	PSO	3.96	14.73	59.25	90.75	81.86
	SAF	0.76	31.23	8.79	66.27	30.50
20~40%	PSO	9.38	23.51	28.36	8.06	6.05
	SAF	3.86	17.31	27.48	10.97	16.76
40~60%	PSO	18.20	24.06	9.18	1.12	5.24
	SAF	14.57	11.57	24.50	9.83	13.84
60~80%	PSO	29.35	18.64	2.16	0.08	3.62
	SAF	36.13	19.42	22.81	8.24	19.29
80~100%	PSO	39.1	19.06	1.04	0	18.53
	SAF	44.68	20.46	16.42	4.69	20.26

4.3. Analyzing the Motion of the Tanker When Towed by the CTV

The tanker is connected to the CTV only through the mooring cables during the operation process in which the CTV synchronously follows the FPSO unit. Figures 15 and 16 show the time–history curves of the relative position and motion of the tanker and the CTV when the headings against waves are 180° and 135°, respectively. Figure 15 shows that when the wave heading is 180°, the tanker moves from the initial position along the starboard direction, and the maximum lateral and longitudinal displacements are 30.64 m and 8.16 m, respectively. Figure 17a shows the test photograph of the slow oscillating motion of the tanker about the initial longitudinal position after the lateral position of the tanker is stabilized near 25 m. Figure 16 shows that when the wave heading is 135°, the tanker moves along the larboard direction, and the maximum lateral and longitudinal displacements of the tanker are 76.65 m and 31.88 m, respectively. The tanker finally stabilizes left and posterior to the CTV under the action of waves and the towing force, as shown by the test photograph in Figure 17b.

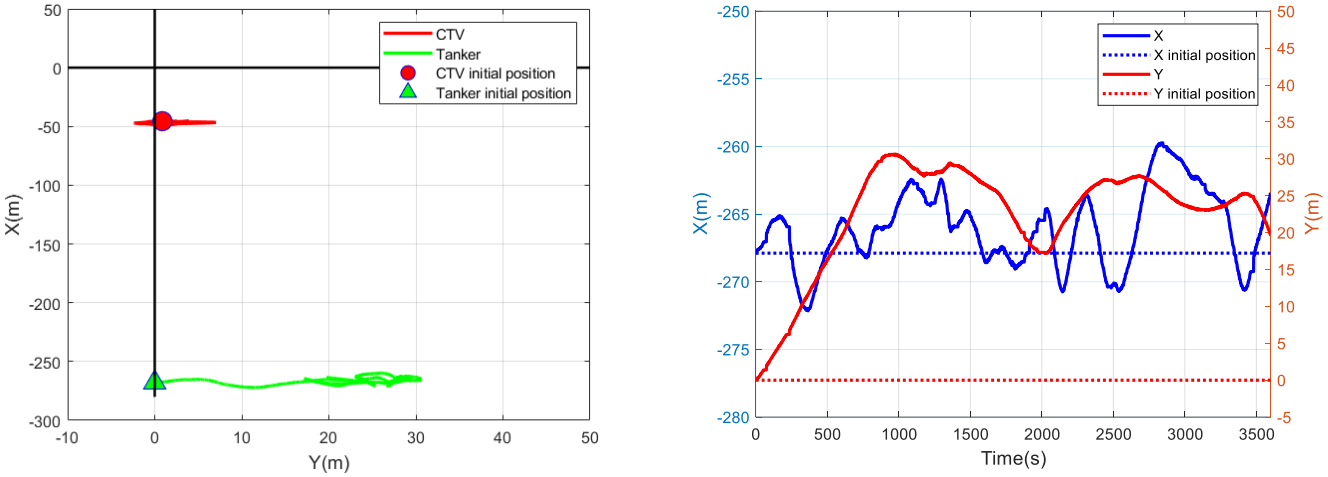

(**a**) (**b**)

Figure 15. Relative position and trajectory of the tanker and the CTV under a wave heading of 180°: (**a**) relative position in the fixed basin coordinate system; (**b**) motion trajectory.

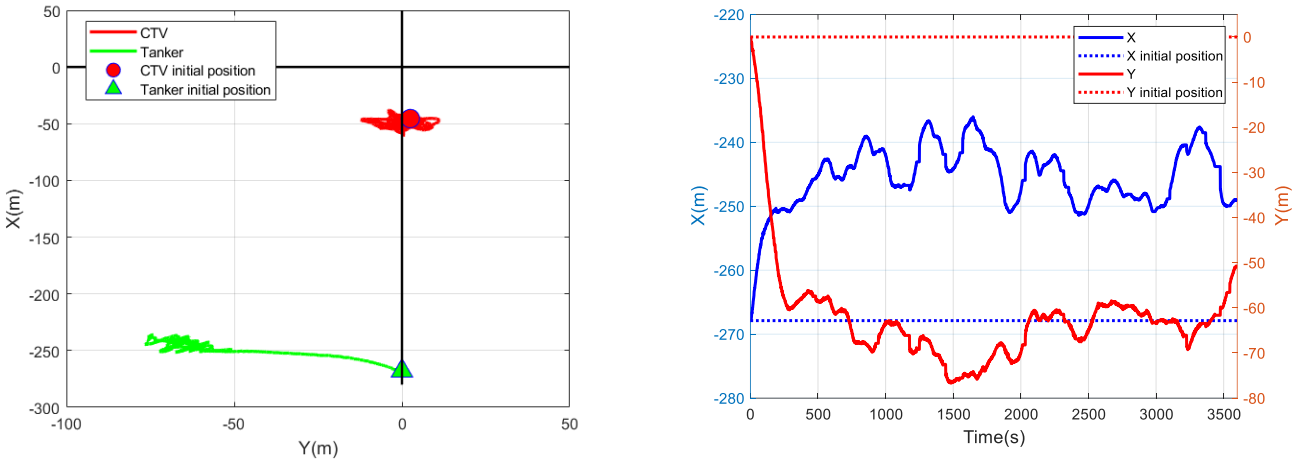

(**a**) (**b**)

Figure 16. Relative position and trajectory of the tanker and the CTV under a wave heading of 135°: (**a**) relative position in the fixed basin coordinate system; (**b**) motion trajectory.

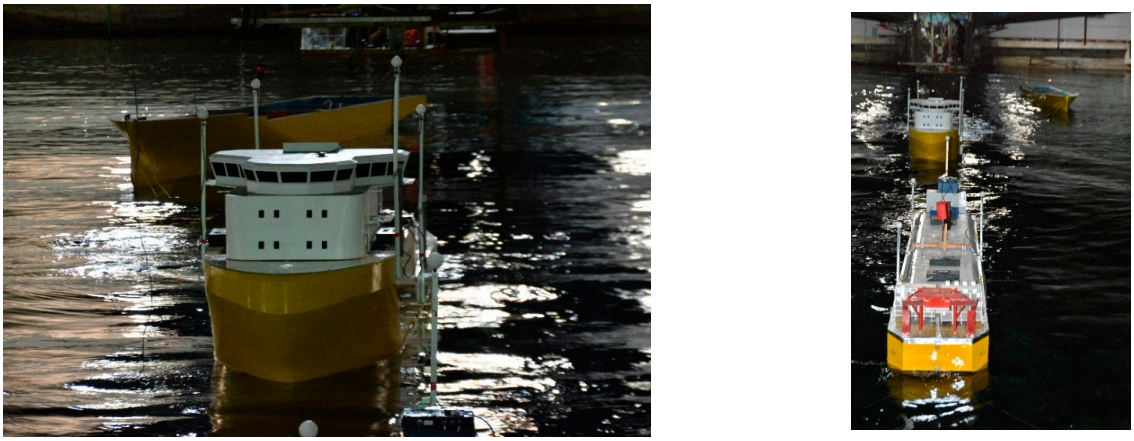

(**a**) (**b**)

Figure 17. Test photographs of the CTV and the tanker under the towing state: (**a**) wave heading is 180°; (**b**) wave heading is 135°.

5. Conclusions

In this paper, an adaptive backstepping synchronous following control strategy based on a virtual leader–follower was proposed for CTV with DP system. A proof was given of the globally exponentially convergence of the closed-loop DP control system by the contraction theorem. In order to generate forces and moments from the DP controller, the thrust allocation of multiple thrusters was considered with an optimal solution method based on the SAF algorithm.

To validate the effectiveness of the proposed control method, model experiments were conducted in irregular waves with different headings against waves. The results verified the capability of the synchronous following control strategy to maintain a safe distance and heading between the FPSO unit and the CTV and clarified the motion characteristics of the tanker under the towing state. Additionally, the results also verified that the DP adaptive backstepping control strategy had strong robustness to different headings against waves. When the wave heading was 180°, the CTV could better maintain a safe working distance from the FPSO unit compared with a wave heading of 135°.

Then, the optimization problem of the desired control commands from the controller was solved through the SAF algorithm, which fully considered the physical characteristics of the azimuth thruster and the thrust forbidden zone caused by the interference between

the thrusters and the ship. The proposed thrust allocation method could fully utilize the rotation rate of the azimuth thruster and effectively solve the high-order truncation error caused in the traditional SQP algorithm through Taylor expansion. When the wave heading was 180°, the actual optimal torque command from the SAF algorithm was almost identical to the control command, with R^2 values of 0.9596 (lateral force), 0.9878 (longitudinal force), and 0.9996 (yaw moment), and the SAF algorithm reduced the maximum and average power consumption compared to the PSO algorithm. When the wave heading was 135°, the wave force and coupled motion significantly increased; however, due to the principle of prioritizing heading control, the SQP, PSO, and SAF allocation algorithms could still meet the control requirements for the yaw moment. Although the power consumption was slightly increased, at this time, the SAF allocation accuracy for the lateral and longitudinal forces significantly increased, with R^2 values of 0.8975 (lateral force), 0.6104 (longitudinal force), and 0.9694 (yaw moment).

Author Contributions: Conceptualization, C.L. and Y.Z.; methodology, C.L. and Y.Z.; software, C.L., L.Z. and Y.T.; validation, C.L., Y.Z. and L.Z.; formal analysis, C.L. and Y.Z.; investigation, C.L. and Y.Z.; resources, C.L., F.T. and Y.Z.; data curation, C.L. and L.Z; writing—original draft preparation, C.L.; writing—review and editing, C.L. and Y.Z.; supervision, M.G. and L.Z.; project administration, C.L.; funding acquisition, C.L. All authors have read and agreed to the published version of the manuscript.

Funding: This research was funded by National Key Research and Development Program of China (grant number 2022YFB3404800) and Natural Science Foundation of Jiangsu Province of China (grant number BK20220222).

Institutional Review Board Statement: Not applicable.

Informed Consent Statement: Not applicable.

Data Availability Statement: Data are contained within the article.

Acknowledgments: We would like to thank to those who helped us in the DP system debug and measurements in scaled model test.

Conflicts of Interest: The authors declare no conflict of interest.

Nomenclature

Abbreviation	Full Name
CSSRC	China Ship Scientific Research Center
DP	Dynamic positioning
CTV	Cargo transfer vessel
FA	firefly algorithm
FPSO	floating production storage and offloading
PSO	particle swarm optimization
R^2	R-squared
SQP	Sequential Quadratic Programming
SAF	self-adaptive firefly
USV	unmanned surface vehicles
Symbol	Description
D_L	linear damping matrix
$H_{1/3}$	significant wave height
I_z	the moment of inertia
M	the mass of the vessel
$N_{\dot{r}}$	added moment of inertia
N_r	hydrodynamic derivative
T_p	spectral peak period
$X_{\dot{u}}$	added masse in x direction
$Y_{\dot{v}}$	added masse in y direction
$Y_{\dot{r}}$	added masses in yaw direction
X_u	hydrodynamic derivative in x direction

Y_v	hydrodynamic derivative in y direction
N_r	hydrodynamic derivative in yaw direction
$N_{\max}$	the maximum number of generations
N_{pop}	the population number
α_0	the step size factor
β_0	attractiveness
γ	light absorption coefficient

Appendix A

Consider a nonlinear system

$$\dot{x} = f(x,t) \tag{A1}$$

where $f(x,t)$ is a continuously differentiable nonlinear function and $x \in \mathrm{R}^n$ is a state vector. Based on the concept of virtual displacement of the system trajectory, if δx denotes the minimum virtual displacement in state x, then the virtual dynamics of system (A1) can be expressed as

$$\delta\dot{x} = (\partial f/\partial x)\delta x \tag{A2}$$

Then,

$$\frac{d}{dt}(\delta x^T \delta x) = 2\delta x^T \frac{\partial f}{\partial x}\delta x \le 2\lambda_{\max}(x,t)\delta x^T \delta x \tag{A3}$$

where the Jacobian matrix J is $\mathrm{J} = \partial f/\partial x$ and $\lambda_{\max}(x,t)$ represents the largest eigenvalue of the matrix $(\mathrm{J}^T + \mathrm{J})/2$.

If $\lambda_{\max}(x,t)$ is uniformly negative definite, then by integrating the two ends of Formula (A3), the length of any infinitesimal virtual displacement $\|\delta x\|$ is found to exponentially converge to 0. If $\delta x^T \delta x$ is expressed as the squared distance of the adjacent trajectories of the system, then all solution trajectories of system (A1) exponentially converge to a certain trajectory, independent of the initial conditions of the system.

Definition A1. *For the system $\dot{x} = f(x,t)$, if there is a region in the state space such that $\mathrm{J} = \partial f/\partial x$ is uniformly negative definite, then the region is called a contracting region.*

Definition A2. *For the system $\dot{x} = f(x,t)$, if any two trajectories starting from different initial conditions exponentially converge to each other, then the system is said to be contracting.*

Lemma A1 ([42]). *For the system $\dot{x} = f(x,t)$, if there is a positive definite matrix $\Theta^T\Theta$ that makes the Jacobian matrix $(\dot{\Theta} + \Theta(\partial f/\partial x))\Theta^{-1}$ uniformly negative definite, then all solution trajectories of the system converge to a certain trajectory, and the system is contracting.*

The results of contraction theory can be extended to various connection systems, and the contractibility of a whole system can be studied through different connection modes of contracting subsystems. Existing connection modes include feedback connections and hierarchical connections. In this paper, the feedback connection mode is used to design the vessel DP contraction controller, so the feedback connection mode will be briefly introduced.

Consider two systems of different dimensions:

$$\begin{aligned} \dot{x}_1 &= f_1(x_1, x_2, t) \\ \dot{x}_2 &= f_2(x_1, x_2, t) \end{aligned} \tag{A4}$$

If coordinate transformation $\delta\mathbf{z} = \Theta\delta\mathbf{x}$ is used, then the following form is satisfied:

$$\frac{d}{dt}\begin{pmatrix} \delta z_1 \\ \delta z_2 \end{pmatrix} = \begin{pmatrix} F_1 & G \\ -G^T & F_2 \end{pmatrix}\begin{pmatrix} \delta z_1 \\ \delta z_2 \end{pmatrix} \tag{A5}$$

If each subsystem is contracting, then the whole system is contracting.

Lemma A2 ([43]). *If the virtual dynamics of system (A1) satisfy the form*

$$\frac{d}{dt}\begin{pmatrix} \delta x \\ \delta \psi \end{pmatrix} = \begin{pmatrix} \partial f/\partial x & G \\ -G^T & 0 \end{pmatrix}\begin{pmatrix} \delta x \\ \delta \psi \end{pmatrix} \tag{A6}$$

and if $\partial f/\partial x$ is negative definite and G is smooth, then system (A1) is asymptotically stable, and ψ is bounded.

References

1. Tan, G.; Zhuang, J.; Zou, J.; Wan, L. Coordination control for multiple unmanned surface vehicles using hybrid behavior-based method. *Ocean Eng.* **2021**, *232*, 109147. [CrossRef]
2. Yan, X.; Jiang, D.; Miao, R.; Li, Y. Formation Control and Obstacle Avoidance Algorithm of a Multi-USV System Based on Virtual Structure and Artificial Potential Field. *J. Mar. Sci. Eng.* **2021**, *9*, 161. [CrossRef]
3. Wu, T.; Xue, K.; Wang, P. Leader-follower formation control of USVs using APF-based adaptive fuzzy logic nonsingular terminal sliding mode control method. *J. Mar. Sci. Technol.* **2022**, *36*, 2007–2018. [CrossRef]
4. Wang, N.; Li, H. Leader-follower formation control of surface vehicles: A fixed-time control approach. *ISA Trans.* **2022**, *124*, 356–364. [CrossRef]
5. Shojaei, K. Leader–follower formation control of underactuated autonomous marine surface vehicles with limited torque. *Ocean Eng.* **2015**, *105*, 196–205. [CrossRef]
6. Cui, R.; Sam, G.S.; Voon, E.H.B.; Sang, C.Y. Leader–follower formation control of underactuated autonomous underwater vehicles. *Ocean Eng.* **2010**, *37*, 1491–1502. [CrossRef]
7. Bouteraa, Y.; Alattas, K.A.; Mobayen, S.; Golestani, M.; Ibrahim, A.; Tariq, U. Disturbance Observer-Based Tracking Controller for Uncertain Marine Surface Vessel. *Actuators* **2022**, *11*, 128. [CrossRef]
8. Witkowska, A.; Śmierzchalski, R. Designing a ship course controller by applying the adaptive backstepping method. *Int. J. Ap. Mat. Com-Pol.* **2012**, *22*, 985–997. [CrossRef]
9. Sun, Z.; Zhang, G.; Lu, Y.; Zhang, W.D. Leader-follower formation control of underactuated surface vehicles based on sliding mode control and parameter estimation. *ISA Trans.* **2018**, *72*, 15–24. [CrossRef]
10. Sun, Z.; Sun, H.; Li, P.; Zou, J. Formation Control of Multiple Underactuated Surface Vessels with a Disturbance Observer. *J. Mar. Sci. Eng.* **2022**, *10*, 1016. [CrossRef]
11. Er, M.J.; Li, Z. Formation Control of Unmanned Surface Vehicles Using Fixed-Time Non-Singular Terminal Sliding Mode Strategy. *J. Mar. Sci. Eng.* **2022**, *10*, 1308. [CrossRef]
12. Sørensen, A.J. A survey of dynamic positioning control systems. *Ann. Rev. Control* **2011**, *35*, 123–136. [CrossRef]
13. Song, W.; Li, Y.; Tong, S. Fuzzy Finite-Time H∞ Hybrid-Triggered Dynamic Positioning Control of Nonlinear Unmanned Marine Vehicles Under Cyber-Attacks. *IEEE. Trans. Intell. Veh.* **2023**, *99*, 1–11. [CrossRef]
14. Chen, H.; Li, J.; Gao, N.; Han, J.; Aït-Ahmed, N.; Benbouzid, M. Adaptive backstepping fast terminal sliding mode control of dynamic positioning ships with uncertainty and unknown disturbances. *Ocean Eng.* **2023**, *281*, 114925. [CrossRef]
15. Zhang, Y.; Liu, C.; Zhang, N.; Ye, Q.; Su, W. Finite-Time Controller Design for the Dynamic Positioning of Ships Considering Disturbances and Actuator Constraints. *J. Mar. Sci. Eng.* **2022**, *10*, 1034. [CrossRef]
16. Alagili, O.; Khan, M.A.I.; Ahmed, S.; Imtiaz, S.; Zaman, H.; Islam, M. An energy-efficient dynamic positioning controller for high sea conditions. *Appl. Ocean Res.* **2022**, *129*, 103331. [CrossRef]
17. Liu, C.; Sun, T.; Hu, Q. Synchronization Control of Dynamic Positioning Ships Using Model Predictive Control. *J. Mar. Sci. Eng.* **2021**, *9*, 1239. [CrossRef]
18. Shi, Q.; Hu, C.; Li, X.; Guo, X.; Yang, J. Finite-time adaptive anti-disturbance constrained control design for dynamic positioning of marine vessels with simulation and model-scale tests. *Ocean Eng.* **2023**, *277*, 114117. [CrossRef]
19. Fujii, S.; Kato, T.; Kawamura, Y.; Tahara, J.; Baba, S.; Sanada, Y. Invention of automatic movement and dynamic positioning control method of unmanned surface vehicle for core sampling. *Artif. Life Robot.* **2021**, *26*, 503–512. [CrossRef]
20. Ianagui, A.S.S.; De Mello, P.C.; Tannuri, E.A. Robust Output-Feedback Control in a Dynamic Positioning System via High Order Sliding Modes: Theoretical Framework and Experimental Evaluation. *IEEE Access* **2020**, *8*, 91701–91724. [CrossRef]
21. Kyrkjebo, E.; Pettersen, K.Y. A virtual vehicle approach to output synchronization control. In Proceedings of the 45th IEEE Conference on Decision and Control, San Diego, CA, USA, 3–15 December 2006.
22. Miller, A. Interaction Forces Between Two Ships During Underway Replenishment. *J. Navig.* **2016**, *69*, 1197–1214. [CrossRef]
23. He, S.; Wang, M.; Dai, S.-L.; Luo, F. Leader–Follower Formation Control of USVs with Prescribed Performance and Collision Avoidance. *IEEE Trans. Ind. Inform.* **2019**, *15*, 572–581. [CrossRef]
24. Guttorm, T. Nonlinear Control and Observer Design for Dynamic Positioning Using Contraction Theory. Master's Thesis, Norwegian University of Science and Technology, Trondheim, Norway, 2004.
25. Zhang, Y.F.; Liu, C.D. Contraction based adaptive backstepping control of dynamic positioning vessels. *Shipbuild. China* **2020**, *61*, 85–94.

26. Alamir, M. Contraction-based nonlinear model predictive control formulation without stability related terminal constraints. *Automatica* **2017**, *75*, 288–292. [CrossRef]
27. Tomera, M.; Podgórski, K. Control of Dynamic Positioning System with Disturbance Observer for Autonomous Marine Surface Vessels. *Sensors* **2021**, *21*, 6723. [CrossRef] [PubMed]
28. Johansen, T.A.; Fossen, T.I. Control allocation—A survey. *Automatica* **2013**, *45*, 1087–1103. [CrossRef]
29. Lindegaard, K.P.; Fossen, T.I. Fuel-efficient rudder and propeller control allocation for marine craft: Experiments with a model ship. *IEEE. Trans. Contr. Syst. Technol.* **2003**, *11*, 850–862. [CrossRef]
30. Ruth, E. Propulsion control and thrust allocation on marine vessels. Ph.D. Thesis, Norwegian University of Science and Technology, Trondheim, Norway, 2008.
31. Li, X.; Yang, L. Study of constrained nonlinear thrust allocation in ship application based on optimization and SOM. *Ocean Eng.* **2019**, *191*, 106491. [CrossRef]
32. Artyszuk, J.; Zalewski, P. Energy Savings by Optimization of Thrusters Allocation during Complex Ship Manoeuvres. *Energies* **2021**, *14*, 4959. [CrossRef]
33. Zhang, L.H.; Peng, X.Y.; Wei, N.X.; Liu, Z.F.; Liu, C.D.; Wang, F. A thrust allocation method for DP vessels equipped with rudders. *Ocean Eng.* **2023**, *285*, 115342. [CrossRef]
34. Xu, S.; Wang, X.; Wang, L.; Li, B. A Dynamic Forbidden Sector Skipping Strategy in Thrust Allocation for Marine Vessels. *Int. J. Offshore Polar Eng.* **2016**, *26*, 175–182. [CrossRef]
35. Kalikatzarakis, M.; Coraddu, A.; Oneto, L.; Anguita, D. Optimizing Fuel Consumption in Thrust Allocation for Marine Dynamic Positioning Systems. *IEEE. Trans. Autom. Sci. Eng.* **2022**, *19*, 122–142. [CrossRef]
36. Arditti, F.; Souza, F.L.; Martins, T.C.; Tannuri, E.A. Thrust allocation algorithm with efficiency function dependent on the azimuth angle of the actuators. *Ocean Eng.* **2015**, *105*, 206–216. [CrossRef]
37. Tang, Z.; He, H.; Wang, L.; Wang, X. An optimal thrust allocation algorithm with bivariate thrust efficiency function considering hydrodynamic interactions. *J. Mar. Sci. Technol.* **2022**, *27*, 52–66. [CrossRef]
38. Gao, D.; Wang, X.; Wang, T.; Wang, Y.; Xu, X. Optimal Thrust Allocation Strategy of Electric Propulsion Ship Based on Improved Non-Dominated Sorting Genetic Algorithm II. *IEEE Access* **2019**, *7*, 135247–135255. [CrossRef]
39. Hou, M.; Yu, M.; Jiao, L. Research on Ship Thrust Distribution Based on Adaptive Particle Swarm Bee Colony Hybrid Algorithm. *J. Phys. Conf. Ser.* **2023**, *2477*, 012088. [CrossRef]
40. Yang, X.S. *Nature-Inspired Metaheuristic Algorithms*, 2nd ed.; Luniver Press: Frome, UK, 2010; pp. 81–89.
41. Liu, J.; Mao, Y.; Liu, X.; Li, Y. A dynamic adaptive firefly algorithm with globally orientation. *Math. Comput. Simul.* **2020**, *174*, 76–101. [CrossRef]
42. Sharma, B.B.; Kar, I.N. Contraction based adaptive control of a class of nonlinear systems. In Proceedings of the American Control Conference, St Louis, MO, USA, 10–12 June 2009.
43. Mohamed, M.; Su, R. Contraction Based Tracking Control of Autonomous Underwater Vehicle. *IFAC-Pap. OnLine* **2017**, *50*, 2665–2670. [CrossRef]